Journal of Materials Chemistry A

PAPER

View Article Online
View Journal | View Issue

Cite this: J. Mater. Chem. A, 2017, 5, 14206

Rational synthesis of Na and S co-catalyst TiO_2-based nanofibers: presence of surface-layered TiS_3 shell grains and sulfur-induced defects for efficient visible-light driven photocatalysis†

Kugalur Shanmugam Ranjith * and Tamer Uyar *

Received 1st April 2017
Accepted 11th June 2017

DOI: 10.1039/c7ta02839c

rsc.li/materials-a

Surface-modified TiO_2 nanofibers (NFs) with tunable visible-light photoactive catalysts were synthesised through electrospinning, followed by a sulfidation process. The utilization of sodium-based sulfidation precursors effectively led to the diffusion and integration of sulfur impurities into TiO_2, modifying its band function. The optical band function of the sulfur-modified TiO_2 NFs can be easily manipulated from 3.17 eV to 2.28 eV through surface modification, due to the creation of oxygen vacancies through the sulfidation process. Sulfidating TiO_2 NFs introduces Ti–S-based nanograins and oxygen vacancies on the surface that favor the TiO_2–TiS_3 core–shell interface. These defect states extend the photocatalytic activity of the TiO_2 NFs under visible irradiation and improve effective carrier separation and the production of reactive oxygen species. The surface oxygen vacancies and the Ti–S-based surface nanograins serve as charge traps and act as adsorption sites, improving the carrier mobility and avoiding charge recombination. The diffused S-modified TiO_2 NFs exhibit a degradation rate of 0.0365 cm^{-1} for RhB dye solution, which is 4.8 times higher than that of pristine TiO_2 NFs under visible irradiation. By benefiting from the sulfur states and oxygen vacancies, with a narrowed band gap of 2.3 eV, these nanofibers serve as suitable localized states for effective carrier separation.

Introduction

In the field of semiconductor photocatalysis, titanium-based nanostructures have attracted much attention for their visible-light response, and have leapt forward in terms of their effectiveness in solar energy applications over the past few decades, due to their superior physical and chemical properties, with peerless efficiency and stability.[1] As a visible-light photocatalyst, TiO_2 has issues relating to its optical responsivity, possessing a wide band gap and underlying electronic structures that impede the utilization of visible-light, resulting in restricted viability.[2–4] The rapid recombination of photo-induced charge carriers is another daunting challenge that curtails its quantum efficiency.[5,6] One of the potential strategies to improve the visible-light catalytic efficiency of TiO_2 is to shift its optical absorption from the UV region to the visible region, allowing more photons to be absorbed and utilized during the decomposition of the pollutants. One dimensional (1D) forms of nanostructures (nanorods, nanotubes, nanobelts, and nanowires, *etc.*) with built-in capacity for the fast collection of photoinduced charge carriers may be potential candidates for improving the chance of enhanced light harvesting, thus enabling TiO_2 to be active in visible region.[7,8] Previous investigations have widely recognized that the efficiency of photocatalytic reactions of TiO_2 nanomaterials can be intensified through doping strategies, which modify the nanomaterial band gap energy and induce dopant energy states in the host lattice.[9–11] However, constructing the heterostructural platform with narrow band gap semiconductors (*e.g.*, PbSe, PbS, CdS, CdTe, CdSe, CuS) can eventually lead to a decrease in the carrier recombination rate and improve the visible-light response of TiO_2.[12] Effective loading of narrow band gap semiconductors onto TiO_2 in the form of core–shell architectures can induce the transition of the optical response from the UV to the visible region, and effectively separate electrons and holes into two different regions of the heterostructural catalyst. Cadmium- and lead-based chalcogenide sensitizers have shown promise in their performances, but they pose environmental concerns, restricting their merits. However, the adept construction of nanoscale TiO_2 heterostructures coupled with other semiconductors has proven itself to be a flourishing attempt towards the enhancement of photocatalytic efficiency and separation of photoinduced charge carriers, exhibiting *in situ* built-in connectivity at the interface with expanded visible-light response, and improved photostability.[13] In light of this, TiS_3,

Institute of Materials Science & Nanotechnology, UNAM–National Nanotechnology Research Center, Bilkent University, Ankara, 06800, Turkey. E-mail: tamer@unam.bilkent.edu.tr; ranjith@unam.bilkent.edu.tr

† Electronic supplementary information (ESI) available. See DOI: 10.1039/c7ta02839c

a fascinating sensitizer with a narrow band gap (E_g < 1.2 eV) comparable to CuS (E_g = 1.9 eV), offers a potential platform to tailor the light absorption in TiO_2 nanostructures.[14] Previously, investigations into the construction of oxide–chalcogenides with a single counterpart (ZnO–ZnS) have revealed improved visible-light catalytic properties, even though both materials have a wide band gap.[15] Oxide–chalcogenides with the same cationic ions can avoid lattice mismatches at the interface, reduce the grain boundary effect and act as a protective layer.[16] Previously, there have been a few interesting reports of TiO_2–metal chalcogenide-based heterostructures for effective hydrogen evolution reactions, which show an effective visible response with improved charge separation.[17] TiS_3 is one promising material in the trichalcogenides family that has huge potential as an electrode material applicable in rechargeable batteries[18] and photoresponsive transistors,[19] with notable optical and electronic properties. Recent theoretical and experimental works have predicted that TiS_3 exhibits an ideal high carrier mobility with a direct band gap and higher stability compared with other trichalcogenides.[20,21] TiS_3 could act as a promising electrode material for rechargeable Li and Na batteries, but in the bulk form, it is necessary to understand the diffusion and volume expansion after Na absorption.[20] Absorption of sodium by TiS_3 may lead to the possibility of the formation of $NaTiS_3$ with a perovskite structure, or a sodium-catalyzed TiS_3-based structure that contributes to the effective tunability of the optical, electrical and band properties of the material. The conferral of multifunctionality due to multiple layers can lead to new and unexpected properties and introduce important novel functionalities. Combining the S-catalyzed TiO_2 or TiS_3 shell layer with TiO_2 in the form of a core–shell heterostructure may promote carrier separation and decrease the recombination rate of photogenerated electrons and holes because of the band position. Furthermore, due to the narrow band function of Ti–S functionalization on the TiO_2 nanoflake (NF) structure, the visible-light response of TiO_2 may improve.[22,23] Additionally, the incorporation of Na impurities in the semiconductor host lattice induces effective carrier mobility and varies the work function of the material.[24,25] Thus, it can modify the band gap of a material and influence it to perform as a p-type semiconductor.[25]

An additional prospect is that the ratio of core material to shell material can be modified by changing the constituents of the core or shell, and the core–shell interface can display a variety of properties depending on the structure and chemical composition of the constituents. The formation of a TiS_3 shell onto a TiO_2 nanostructure leads to the avoidance of fast carrier recombination in the core–shell heterostructure, providing support for the separation of photoinduced charge carriers through the core–shell interface. Thus, it is envisaged that integrating sulfur modification in the form of a TiS_3 shell on the TiO_2 nanostructure reveals a type-II system that exhibits commendable photocatalytic efficiency and substantial retardation in the recombination rate of photoinduced charge carriers, which are of prime relevance in the field of photocatalysis. From the above analysis, we report the design and synthesis of Na co-catalyst type-II TiO_2–TiS_3 core–shell nanostructures through a surface sulfidation process, for the first time. These core–shell nanostructures exhibit commendable visible-light driven photocatalytic performance for the degradation of harmful organic pollutants in wastewater.

To highlight the merits of incorporating Na into TiO_2–TiS_3 core–shell nanostructures, we also designed TiO_2–TiS_3 core–shell nanofibers under similar conditions (instead of Na_2S we used thioacetamide (TAA) as the sulfidation precursor). The favorable photocatalytic performance of the Na co-catalyst TiO_2–TiS_3 core–shell nanofibers over the TiO_2–TiS_3 core–shell nanostructures was scrutinized in terms of Na functionalization, which enables closer contact on TiS_3 and $NaTiS_3$ may form as a perovskite shell layer over the TiO_2 nanofiber surface, facilitating the efficient separation of photoinduced charge carriers. Our work also unveils the admirable stability and recyclability of the Na co-catalyst core–shell nanostructured photocatalyst. The co-catalyst functionality supports the conclusion that this material has potential as a viable and stable photocatalyst for environmental applications. We thus anticipate that our results reveal its broad potential as a catalyst under visible irradiation with stable and reusable functionality.

Experimental

Materials

Polyvinylpyrrolidone (PVP, M_w = 1 300 000, Sigma-Aldrich), titanium tetra butoxide ($Ti(OBu)_4$, Sigma-Aldrich) acetic acid (CH_3COOH, Sigma-Aldrich), ethanol (99.8%, C_2H_5OH, Sigma-Aldrich), sodium sulfate (98%, Na_2S, Alfa Aesar), thioacetamide (98%, TAA, Alfa Aesar), methylene blue (MB, Sigma-Aldrich), rhodamine B (RhB, Sigma-Aldrich), 4-chlorophenol (99%, 4-CP, Alfa Aesar), nitroblue tetrazolium chloride (NBT, Alfa Aesar), terephthalic acid (98%, TA, Sigma-Aldrich), and Degussa P25 were procured and used as received without any further purification.

Synthesis of TiO_2 nanofibers

The synthesis of TiO_2 nanofibers was accomplished through an electrospinning process. To prepare the precursor solution, 0.5 g of polyvinylpyrrolidone (PVP, M_w = 1 300 000, Sigma-Aldrich) was dissolved in 2.5 ml of ethanol by stirring. Titanium tetra butoxide ($Ti(OBu)_4$) (0.5 ml) was used as a Ti precursor and was stirred for 20 min in 1 ml of ethanol and 0.3 ml of acetic acid. This solution was then added to the polymer solution. After stirring for 3 h, the precursor solution was drawn into a 3 ml plastic syringe with a needle of 0.4 mm in diameter. The needle tip was placed into an electrospinning system (KD Scientific, KDS101) at a flow rate of 0.5 ml h^{-1}; the distance between the tip of the needle and the grounded aluminum plate was approximately 15 cm. The needle was connected to a high-voltage power source, and a voltage of 15 kV was applied from a high voltage power supply (Spellman, SL series, USA). The electrospun TiO_2/polymer nanofibers were dried at 80 °C in an oven for 6 h and then calcined at 500 °C for 3 h in air.

Synthesis of S-catalysed TiO_2 and TiO_2–TiS_3 core–shell nanofibers

The conversion of the TiO_2 nanofibers into TiO_2–TiS_3 core–shell nanofibers was carried out by immersing or dispersing the TiO_2 nanofibers in 30 mM TAA solution and hydrothermally treating at 120 °C for 16 h to create a thin TiS_3 shell layer around the TiO_2 nanofibers through sulfidation (S-TiO_2 NFs). The final product was washed with distilled water and then dried at room temperature. TiO_2–TiS_3 core–shell nanofibers were fabricated as a hierarchical photocatalyst through annealing at 200 °C under vacuum for 2 h. At 8 h of sulfidation, there was a trace of S impurities on the TiO_2 surface, while after 16 h there was no notable variation in the presence of S impurities on the NF surface. Hence, the sulfidation time was fixed at 16 h for the surface modification.

Synthesis of Na and S co-catalyst TiO_2 and Na catalyst TiO_2–TiS_3 core–shell nanofibers

To incorporate Na in the TiO_2–TiS_3 core–shell nanofibers, instead of using TAA solution as a sulfidation source, Na_2S was used to form TiO_2–TiS_3 core–shell nanofibers under the above preferred conditions (Na/S-TiO_2 NFs). In this process, the Na by-product diffuses through the TiO_2 surface and forms a co-catalyst with sulfur on the surface of the TiO_2 nanofibers. The final product was washed using deionized water and then dried at room temperature and annealed under vacuum. To elucidate the primary role of Na over the TiO_2 surface, 0.25 mM of sodium hydroxide was dissolved in 40 ml of water dispersed with 50 mg of TiO_2 nanofibers, and the mixture was hydrothermally treated at 120 °C for 4 h, washed and dried (Na–TiO_2 NFs).

Characterization

The morphologies of the as-synthesized and sulfidated nanofibers were investigated using a scanning electron microscope (SEM, FEI-Quanta 200 FEG). To identify the composition and phase of the samples, X-ray diffraction (XRD) patterns were recorded on a PANalytical X'pert multipurpose X-ray diffractometer. Raman spectra were collected on a WITec confocal Raman spectrophotometer (equipped with He–Ne laser, excitation wavelength of 532 nm) for the microstructural investigation of the samples. Transmission electron microscopy (TEM) imaging was carried out on a FEI-Tecnai G2 F30 to examine the morphologies and sizes of the sample. Energy-dispersive X-ray spectroscopy (EDX) was carried out on the TEM instrument. To detect the chemical composition and electronic structure, X-ray photoelectron spectroscopy (XPS) analysis was conducted using a Thermo K-alpha-monochromated X-ray photoelectron spectrometer with Al Kα radiation as the excitation source ($h\nu$ = 1484.6 eV) and carbon (284.6 eV binding energy) was used as a reference to correct the binding energy of the sample. UV-vis diffuse reflectance spectra were measured on a UV-3600 (Shimadzu, Japan) spectrophotometer. A transformed Kubelka–Munk relation, $(F(R_\infty)h\nu)^{1/2}$, is plotted against $h\nu$, and the extrapolation of $(F(R_\infty)h\nu)^{1/2}$ to zero $F(R_\infty)$ calculates the band gap energy, unravelling the light harvesting ability of the samples. Elemental mapping was examined using EDX analysis on a scanning transmission electron microscope (STEM, Tecnai G2 F30, FEI). The fluorescence spectra of the samples were taken at room temperature on a photoluminescence (PL) spectro fluorometer (time-resolved fluorescence spectrophotometer FL-1057 TCSPC) with an excitation wavelength at 350 nm. The specific surface area of the samples was analyzed using the Brunauer–Emmett–Teller (BET) method, carried out on a Quantachrome Instrument autosorb (iq_2) analyser after degassing the samples for 3 h at 200 °C.

Photocatalytic properties

The evaluation of the photocatalytic performance of the Na co-catalyst TiO_2–TiS_3 core–shell nanofibers and their bare and single catalyst counterparts (TiO_2 and Na–TiO_2) was explored by scrutinizing the degradation of RhB, a virulent organic pollutant of dye wastewater, under UV (Ultra-Vitalux Ultraviolet high pressure lamp, 300 W, Osram, sunlight simulation) and visible irradiation (75 W, Osram, Xenon lamp with UV filter) at room temperature. Typically, 1 mg ml^{-1} of electrospun TiO_2-based NF structures was placed into a quartz cuvette containing RhB dye solution (15 ppm), and then the cuvette was placed in the dark for 20 minutes to establish the adsorption/desorption equilibrium of dye on the sample surface prior to irradiation. The samples were placed at a working distance of 15 cm from the lamp. A series of samples and controls (without catalyst) were simultaneously irradiated. Blank experiments were executed in the dark to study the role of photon energy in the degradation of RhB. The degradation of RhB dye was monitored by measuring its absorbance as a function of irradiation time at predetermined time intervals using a UV-vis spectrophotometer. For comparison, the catalytic activity of commercially available Degussa P25 was observed and compared with the sulfidated TiO_2 NFs. The reusability of the sample was tested over five consecutive cycles. The degradation efficiency of RhB dye was calculated using the equation $((C_0 - C)/C_0) \times 100$, where C and C_0 indicate the absorption peak intensities before and after photo-irradiation, respectively. Additionally, the photocatalytic properties were investigated and compared with another dye (MB, 15 ppm) and colorless organic waste (4-CP, 10 ppm).

Analysis of superoxides and hydroxyl radicals

The method presented here is similar to that of the photocatalytic activity test. NBT (100 mM, exhibiting an absorption maximum at 259 nm) was used as the indicator to determine the amount of $O_2^{\bullet -}$ generated by the nanocatalyst[26] and the brief procedure is given in the ESI.† The formation of hydroxyl radicals ($^{\bullet}OH$) on the surface of Na and S co-catalyst TiO_2 NFs was detected by PL using terephthalic acid as the probe molecule. A 75 W Xe lamp was used as the light source. The experimental procedure was similar to that used in the measurement of photocatalytic activity, except that the aqueous solution of RhB was replaced by an aqueous solution of 5×10^{-4} M terephthalic acid and 2×10^{-3} M NaOH. The visible-light irradiation was continuous and sampling was performed at given

time intervals for analysis. The solution was analyzed after filtration on a PerkinElmer LS55 fluorescence spectrophotometer. The product of the terephthalic acid hydroxylation, 2-hydroxyterephthalic acid, gave a peak at a wavelength of about 425 nm by excitation with a wavelength of 315 nm. The intensity of the 425 nm PL peak increased with increasing irradiation.[26]

Stability and recyclability of Na co-catalyst TiO_2–TiS_3 core/shell photocatalyst

To evaluate the stability and recyclability of the photocatalyst, five successive runs of the photodegradation process were performed. Following the completion of each run, the photocatalyst was recycled by washing it with water and absolute alcohol and then drying at 70 °C for the next cycle of photocatalysis. The stability of the photocatalyst was scrutinized through SEM and XPS studies.

Results and discussion

The fabrication of 1D S and Na co-catalyst TiO_2 nanofibers was realized *via* the sulfidation of electrospun TiO_2 nanofibers with TAA and Na_2S precursors. Fig. 1 shows SEM images of the pristine, Na, S and Na/S-TiO_2 nanofibers, which offer insights into the morphology and surface features of the resultant samples. The SEM image of the as-electrospun PVP/titanium iso-butoxide composite NFs clearly shows a bead-free and smooth fibrous nature with an average fiber diameter of 450 ± 85 nm, as shown in Fig. S1.† Furthermore, the as-prepared composite nanofibers were subjected to annealing at 500 °C to form TiO_2 NFs by completely degrading the organic part (PVP polymer matrix and impurity groups). The obtained TiO_2 NFs were subjected to a sulfidation process in order to modify the TiO_2 NF surface with Na and S ions. Additionally, to understand the individual role of Na and S ions, single-ion S-TiO_2 and Na–TiO_2 NFs were designed by modifying the sulfidation precursor and diffusing Na over the TiO_2 NFs. Our present study investigates the effect and role of Na and S ions on the TiO_2 NFs for effective photocatalysis under UV and visible irradiation. The morphological characterizations clearly reveal the substantial role of Na and S ions on the TiO_2 surface. Even after the post-calcination process, the fibrous surfaces were smooth, and the effective substitution of Na played a vital role in the surface modification of the TiO_2 NF surface. After annealing at 500 °C, the TiO_2 NFs with diameters of 150 ± 50 nm revealed a closely packed grain assembly, as shown in Fig. 1a and b. Fig. 1c–f show the SEM images of the NF samples obtained under the different sulfidation precursors at a reaction time of 16 h, which clearly demonstrate the change in the surface morphology of the NFs with respect to the sulfidation precursors. Compared to the pristine TiO_2 NFs, there is no notable surface morphological change over the sulfidated NFs using TAA (Fig. 1c and d). However, upon using Na_2S as the sulfidation precursor, noticeable surface modification was observed on the TiO_2 NF surface with the advent of porous features, highlighting the role of Na on the S-modified surface of the TiO_2 NFs (Fig. 1e and f). From Fig. 1g and h, it can be observed that Na alone influenced

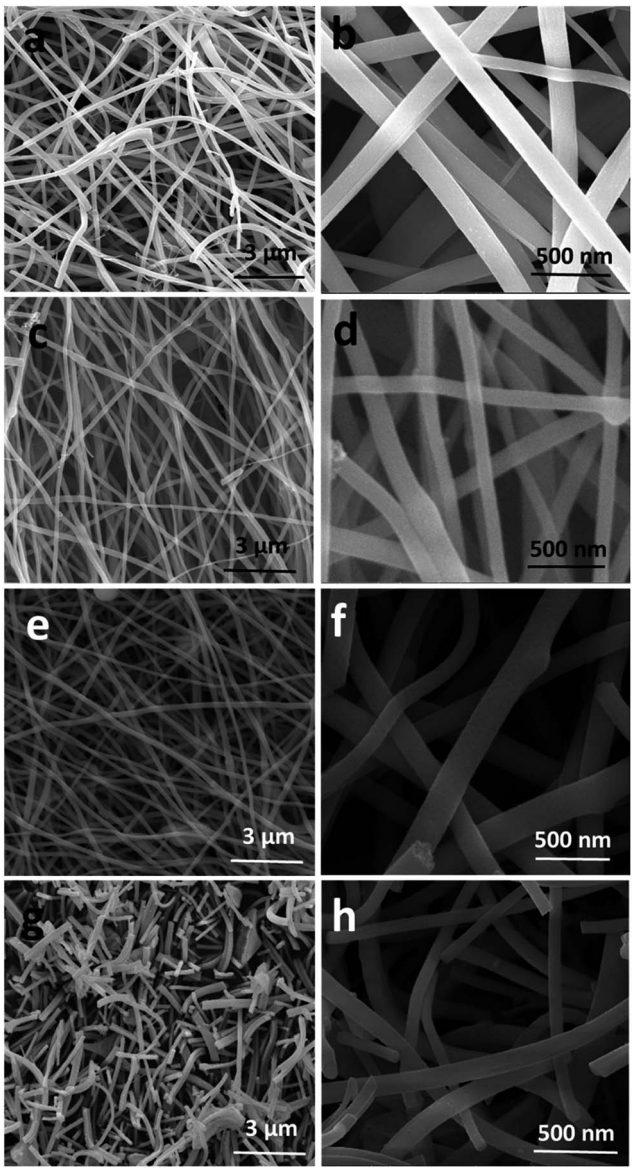

Fig. 1 SEM micrographs of (a and b) pristine TiO_2 NFs, (c and d) S-TiO_2 NFs (through TAA solution), (e and f) Na/S-TiO_2 NFs (through Na_2S solution) and (g and h) Na–TiO_2 NFs (Na through a hydrothermal process).

the morphological change on the TiO_2 NFs. Upon comparison with the sulfidated TiO_2 NFs, the Na–TiO_2 NFs exhibited a broken nature in their fiber morphology. The considerable increase in surface roughness under the influence of Na ions reveals the diffusion of Na through a reaction process on the TiO_2 NF surface. The EDS spectra of the Na/S-TiO_2 NFs reveal the presence of Na and S ions on the TiO_2 surface (Fig. S2†).

The presence of sulfur was due to the formation of the Ti–S on the surface. The formation mechanism of the TiO_2–TiS_3 core–shell NFs cannot be fully understood, but through the Kirkendall process, it might be explained in terms of diffusive migrations among different atomic species in metals and/or alloys through thermal activation. Fig. 2 shows the powder X-ray diffraction (PXRD) data of pristine and sulfidated TiO_2

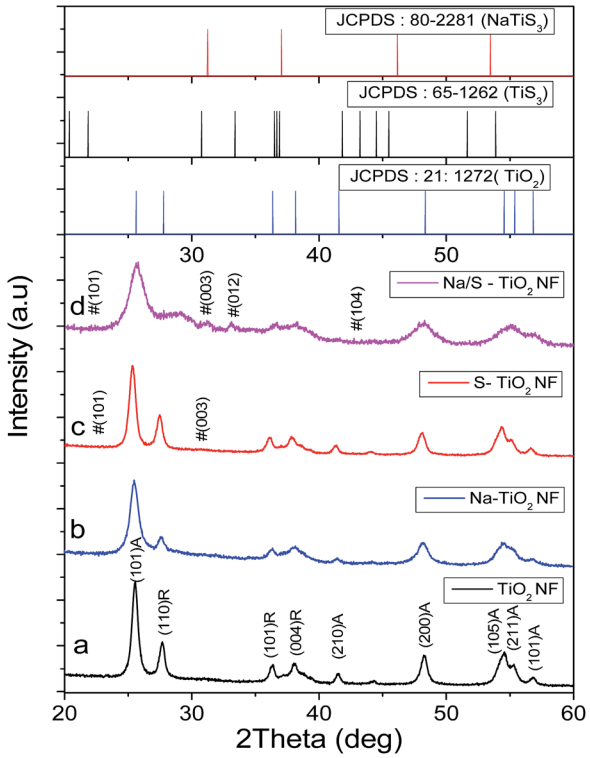

Fig. 2 XRD patterns of (a) pristine TiO_2 NFs, (b) Na–TiO_2 NFs, (c) S-TiO_2 NFs and (d) Na/S-TiO_2 NFs.

NFs, along with the identification of the phase composition and structure characterization. In Fig. 2a, the XRD pattern of the pristine TiO_2 NFs reveals the prominent anatase phase with mild substitution of rutile corresponding to the JCPDS card: 21-1272. Sulfidated TiO_2 NFs in TAA precursor exhibit similar spectral peaks to those of pristine TiO_2 NFs, with additional mild traces of TiS_3 peaks at 21.84°, 30.78° and 33.41°, which provide evidence for the formation of TiS_3 with monoclinic phase (JCPDS no. 65-1262). However, these peaks do not clearly confirm the formation of a TiS_3 shell layer, because instead of forming TiS_3, a certain amount of S may have modified the TiO_2 surface due to H_2S interaction on the TiO_2 surface. During the incorporation of S and Na in TiO_2 using Na_2S for the sulfidation precursor, the XRD pattern reveals that upon sulfidating the TiO_2 NFs with Na_2S, the rutile phase of the TiO_2 starts to decay and a trace amount of TiS_3 was confirmed by the presence of additional peaks at 21.84°, 30.78° and 33.41°, which can be unquestionably assigned to the monoclinic phase of TiS_3 (JCPDS no. 65-1262) with improved FWHM in the diffraction spectra. The absence of the spectral peaks of $NaTiS_3$ and other additional peaks clearly reveals the formation of the TiO_2–TiS_3 crystal structure.

The unveiled shift in the reflections corresponding to TiO_2 toward larger angles reveals the lattice compression of TiO_2 with TiS_3 shell structural modification through the sulfidation process. The conversion of the TiO_2 surface through S and Na modification discloses the contraction of the lattice planes of TiO_2 and thus lowers the lattice constant of TiO_2 in the TiO_2–TiS_3-modified nanostructures, as compared to the pristine TiO_2 NFs. Nevertheless, the absence of a shift in the spectral reflections of the Na–TiO_2 NFs reveals the effective role of S ions on the TiO_2 surface. Thus, from the PXRD studies, we infer anatase and monoclinic phases for TiO_2 and TiS_3, respectively, in the form of TiO_2–TiS_3. However, the convincing evidence of the core–shell geometries in the TiO_2–TiS_3 nanostructures is furnished by additional studies described below.

The Raman characteristic peaks of TiO_2 and Na/S-TiO_2 NFs were observed at about 148, 194, 241, 391, 508 and 628 cm^{-1}, corresponding to $E_{g(1)}$ and E_g, second-order scattering, and $B_{1g(1)}$, A_{1g} + $B_{1g(2)}$ and $E_{g(2)}$ modes of anatase, respectively (Fig. S3†).[27] It was evident that, after Na and S modification, the TiO_2 NFs were in the anatase phase. These peaks represented O–Ti–O bending-type vibrations and Ti–O bond stretching-type vibrations. Also, the observed $B_{1g(1)}$, A_{1g} + $B_{1g(2)}$ and $E_{g(2)}$ peaks of the modified TiO_2 NFs were slightly shifted in comparison with the bare TiO_2, indicating the formation of a hybrid structure between Na and S in the TiO_2 NFs. Significantly, the presence of an additional peak at around 600 cm^{-1} corresponds to the presence of S-based impurities on the TiO_2 NFs.[28] The inset shows expanded views of the E_g Raman band at 147 cm^{-1}. It is found that the E_g band in pristine TiO_2 shifts to a higher wavenumber under the influence of sulfidation, indicating the incorporation of S into the TiO_2 crystal lattice. This may also be due to the reduction in particle size during the sulfidation. A decrease in the grain size influences the vibrational properties of the material, and size-induced radial pressure would lead to an increase in the force constants due to the reduction in the interatomic distance. Thus, the Raman spectral results are consistent with the XRD observations shown in Fig. 2.

The solid structural features and the closed compressed assembly of nanograins reveal the solid core nature of the TiO_2 NFs (Fig. 3a and b). The selected area diffraction (SAD) pattern (Fig. 3a, inset) and the high-resolution TEM (HRTEM) (Fig. 3c) image show the structural and crystalline nature of a pristine TiO_2 NF. The NF has a diameter of around 160 nm with compressed nanograins throughout the entire fiber. The HRTEM and SAED pattern of the pristine TiO_2 NF reveal the

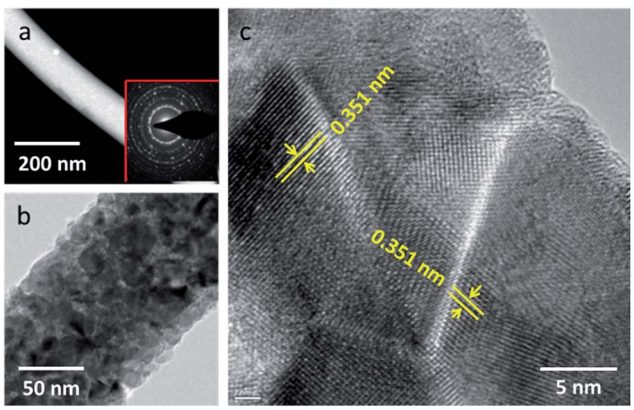

Fig. 3 STEM (a), TEM (b) and HRTEM (c) images of pristine TiO_2 NFs. Inset shows the SAED of the respective image.

polycrystalline nature of TiO_2 and the lattice spacing of 0.351 nm over the surface area correlates to the (101) plane of anatase TiO_2 (JCPDS PDF: 21-1272) (Fig. 3b and c). TEM and HRTEM images of a sulfidated TiO_2 NF precisely show the existence of TiS_3 nanograins on the NF surface (Fig. 4). Fig. 4a shows TEM images of the NF exhibiting a distribution of TiS_3 from the sulfidation process using the TAA precursor. The TEM images unveil the random decoration of TiS_3 nanograins with an average thickness of ~5 nm on the surface of the TiO_2 NFs. There is no significant contrast between the TiO_2 core and TiS_3 shell region that may confirm the existence of core–shell geometry. However, the presence of two sets of lattice fringes with spacings of 0.410 and 0.351 nm in the surface region, respectively evidences the dual presence of TiS_3 and TiO_2 nanograins on the fiber surface. The lattice spacing of 0.351 nm on the surface area correlates to the (101) plane of anatase TiO_2, and the sulfidated grains having a spacing of 0.410 nm agrees well with the (011) plane of monoclinic TiS_3. The inset shows the selected area electron diffraction (SAED) pattern of TiS_3 with the TiO_2 nanograins, indicating the polycrystalline nature of the samples. Fig. 4b shows typical TEM images of the TiO_2–TiS_3 system sulfidated using the Na_2S precursor. The rough surface with the dislocated grain assembly of the NF network reveals the surface modification during the sulfidation process (Fig. 4b). HRTEM images of the surface grains reveal a line spacing of 0.480 nm, which agrees very well with the distance along the *a*-direction of the TiS_3 lattice in the (011) crystal plane. The inset SAED pattern reveals the polycrystalline nature of the samples and indicate a change towards amorphous nature due to Na diffusion, which can explain the amorphous surface observed in the HRTEM results. However, in the HRTEM studies of both different sets of sulfidation processes, the 1D NF network does not give the picture of a perfect core–shell architecture, but in the whole area, the surface clearly shows a composite geometry with TiO_2–TiS_3 nanostructures. Thus, the TEM and HRTEM studies unambiguously support the existence of two types of S and Na/S-TiO_2 NFs with surface-decorative functionality, such as core–shell geometry.

Energy dispersive X-ray spectroscopy (EDS) mapping studies reveal the elemental composition and its distribution on the NFs. The results of the mapping studies (Fig. 4a3–a7 and b3–b7) of the S and Na/S-TiO_2 NFs portray the coexistence of Ti, O and S

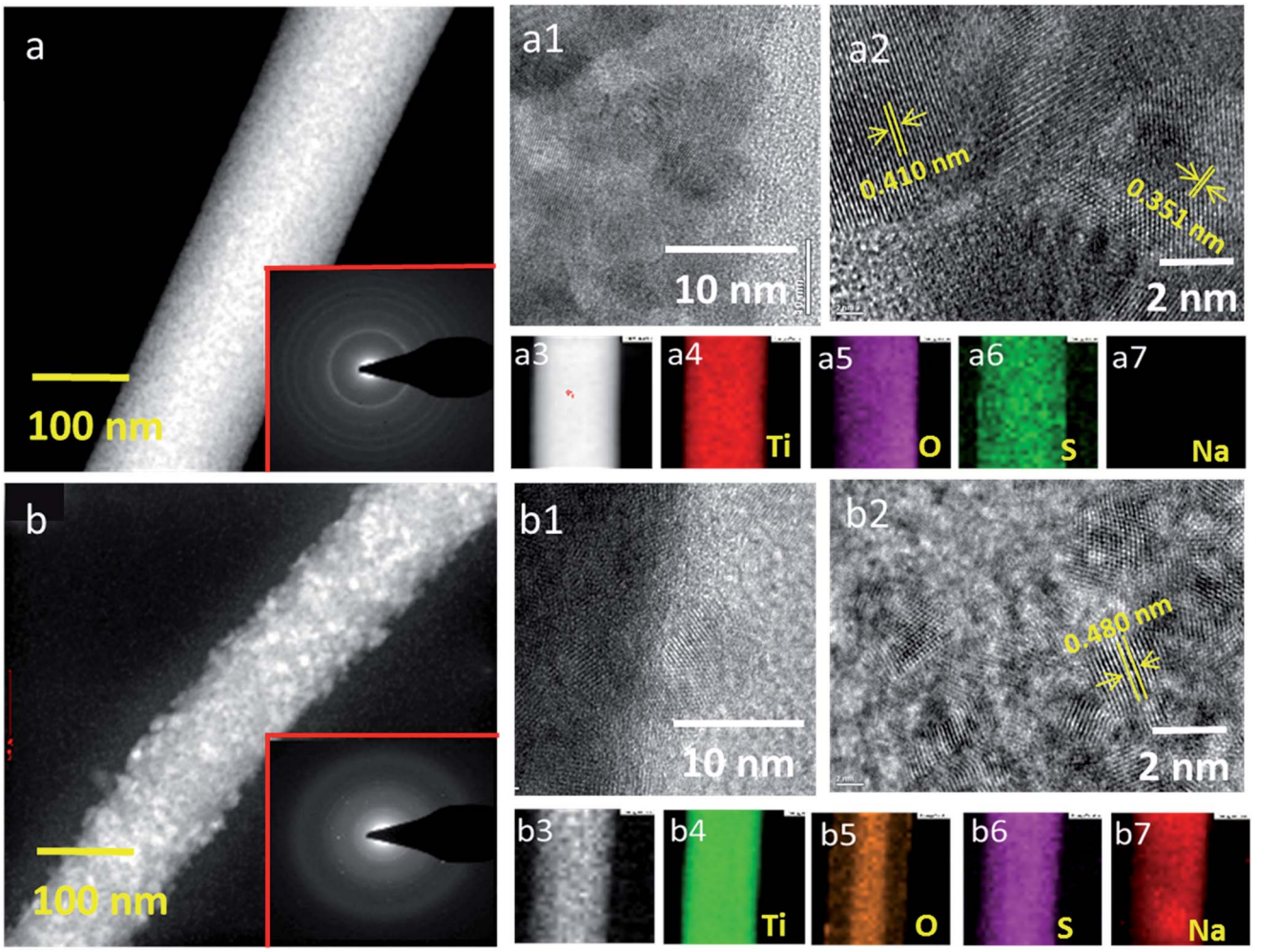

Fig. 4 (a and b) STEM, (a1 and b1) TEM and (a2 and b2) HRTEM images of the S-TiO_2 NFs and Na/S-TiO_2 NFs, respectively. Elemental mapping results of (a3–a7) S-TiO_2 NFs and (b3–b7) Na/S-TiO_2 NFs. Inset shows the SAED of the respective S-TiO_2 NFs and Na/S-TiO_2 NFs.

elements. Using TAA as a precursor, the distribution of S was homogeneous all over the surface of the TiO_2 NFs. The results obtained from the TEM and HRTEM studies support the fact that the TiS_3 nanograins uniformly covered the TiO_2 core of the NFs with a thickness of nearly 10 nm. Fig. 4b3–b7 show the elemental mapping studies of the TiO_2–TiS_3 nanostructures sulfidated using the Na_2S precursor, and illustrate the coexistence of Ti, O, Na and S elements. Noticeably, the distribution of S and Na was uniform and these elements had diffused into the NF system to a depth of nearly 30 nm. The results show that Na had diffused through the NF surface and favored an extended path for the S ions to interact with TiO_2. Mapping studies convey the homogeneous distribution of S and Na on the surface and the effect of Na on the TiO_2 surface. However, the basic nature of the nanograin assembly of the NF network does not reveal the clear core–shell geometry of the TiO_2–TiS_3 nanostructures. The coexistence of TiO_2 and TiS_3 crystalline grains after the sulfidation process indicates the incomplete or slower sulfidation of TiO_2. This evidences that TiO_2 can be deformed or converted into TiS_3 through sulfidation, but the sulfidation will be extendable if the S ions diffuse through the inner core of the fibers. Due to the diffusion ability of Na, a pathway for sulfur diffusion through the inner core is made possible, which enhances the co-existence of TiO_2/TiS_3 nanograins and forms the heterojunction interface, which may enhance the separation efficiency of electrons and holes, thus improving the photocatalytic performance. The specific BET surface area of the TiO_2 NFs, S-TiO_2 NFs and Na/S-TiO_2 NFs was determined to be 14.894 $m^2\ g^{-1}$, 19.564 $m^2\ g^{-1}$, and 29.986 $m^2\ g^{-1}$, respectively. From the comparative isotherm results (Fig. S4†), the Na/S-TiO_2 NFs apparently exhibit an increase in the surface area, compared to the pristine TiO_2 NFs and S-TiO_2 NFs, because of the creation of a rougher surface due to the diffusion of S and Na ions.

The surface chemical composition and chemical states of the sulfidated TiO_2 NFs were investigated by XPS as a function of different sulfidation precursors. The full scan spectrum reveals the presence of Ti, O, S and C ions on surface-modified TiO_2 NFs under their respective binding energies (Fig. S5†). The presence of C can be ascribed to carbon-based contaminants acquired during the synthesis process. The presence of a higher intensity at the binding energy of 284.7 eV represents the C–C bonding of carbon atoms (Fig. S5†). There is a possibility that C doping occurred during the synthesis process, which was revealed by the trace signal at 283 eV associated with the Ti–C bonds connected to oxygen vacancies.[29] The Fig. 5a shows the high-resolution scan of the Ti 2p profile spectrum of the TiO_2 NFs with respect to the different sulfidation processes. The Ti 2p spectrum reveals that the pristine NFs exhibit peaks at 458.5 and 464.3 eV, which correspond to Ti $2p_{3/2}$ and Ti $2p_{1/2}$, respectively. The spacing between the Ti $2p_{3/2}$ and Ti $2p_{1/2}$ lines was 5.8 eV, suggesting the existence of the Ti^{4+} oxidation state.[30] With respect to the sulfidation process, the shift of Ti $2p_{3/2}$ indicates the presence of Ti^{3+},[31] while the notable split in the $2p_{3/2}$ spectrum in the sulfidated samples reveals the presence of Ti^{4+} and Ti^{3+} species on the surface. The existence of Ti^{3+} with a substitution ratio of Ti^{4+}/Ti^{3+} in TiO_2 would induce the oxygen vacancies to maintain electrostatic balance in the crystal structure.[32] Additionally, the shift towards higher binding energies on the sulfidated samples indicates a lower electron density at the surface, which suggests the interaction of S ions with the surface. The higher resolution scanning of O 1s spectra with the Gaussian function, with respect to the different sulfidation processes are shown in Fig. 5b. The Gaussian function with the two split fitted peaks denotes the presence of two different O species, namely, lattice oxygen (O_L), and non-lattice oxygen such as oxygen vacancies (O_V).[30] It can be seen that the intensity of O_V centered at 531 ± 0.4 eV is promoted due to the sulfidation process. The change in the ratio of oxygen vacancies may be due to the existence of Ti^{3+} and the formation of TiS_3 nanograins and the calculated relative percentages of O_L and O_V for all the samples are noted in Table S1.† A decrease in the

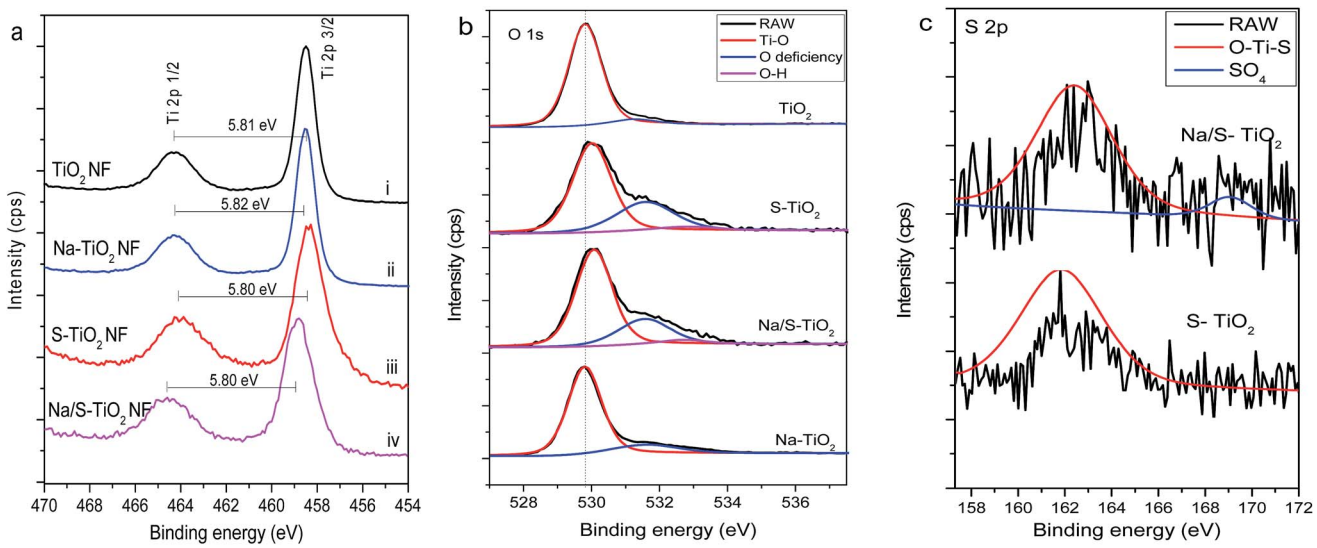

Fig. 5 XPS spectra of the pristine TiO_2 NFs and surface-modified TiO_2 NFs samples: (a) Ti 2p; (b) O 1s; (c) S 2p.

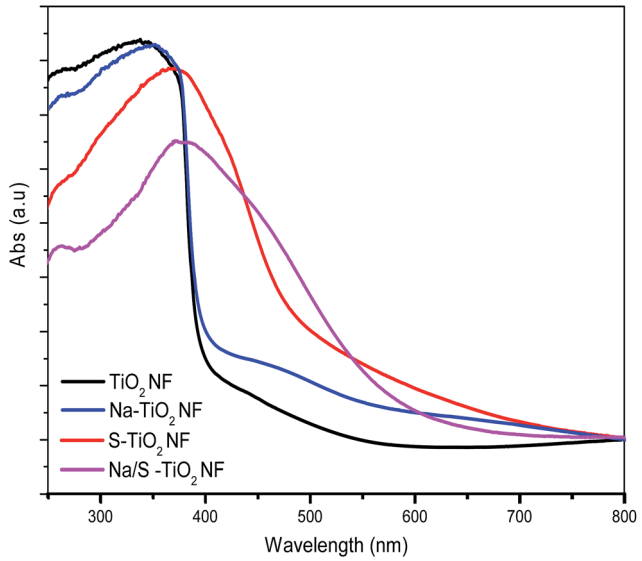

Fig. 6 UV-Vis DRS absorbance spectra of pristine TiO_2 NFs and surface-modified TiO_2 NF samples.

presence of O_L during sulfidation indicates the interaction of S ions with Ti–O and the weak bonding of Ti–O. Fig. 5c presents the high-resolution scanning S 2p spectra of the sulfidated TiO_2 NFs. The signal at around 162.2 eV represents S^{2-}, attributed to the interaction of S ions with Ti. Additionally, NFs sulfidated in the presence of the Na_2S precursor exhibit SO_4 functionality (at 168.4 eV), which highlights the interaction of trace oxygen ions with S ions. However, this was not observed in the TAA-based sulfidation process. The broad appearance of the S 2p peaks at 162.2 eV was attributed to S $2p_{3/2}$ and S $2p_{1/2}$, ascribed to the hybrid chemical bond species of S^{2-} and Ti–S.[33] By inducing ion etching on the sulfidated NFs, the intensity count was reduced and revealed the absence or a very minor trace of S^{2-} ions, indicating that the S ions were decorated only on the surface of the TiO_2 NFs (Fig. S6†). The sulfate ions interact as the nature of the O–S–O bond induces the imbalance of charge on the Ti and vacancy sites on the TiO_2 NFs.[34] Further S^{6+} and S^{4+} serve as surface traps for photoinduced electrons and holes, which suppresses the carrier recombination.[35] These results demonstrate the presence of S-modification on the TiO_2 NF surface, and by using different sulfidation precursors, the surface chemistry of the TiO_2–TiS_3 NFs was effectively varied. Although the broad peak observed at 1073 eV may point to Na presence, we cannot precisely pin to Na 1s, because the Ti LMM peaks will also appear in the same position (Fig. S7†).

Fig. 6 and S8† show the optical absorption behavior and calculated band gap energy of the Na- and S-functionalized TiO_2 NFs, through diffuse reflectance spectroscopy (DRS) studies. Bare TiO_2 NFs unveil a sharp absorption edge in the UV region corresponding to a band gap of 3.14 eV through the transfer of valence band electrons to the conduction band. The DRS profile for Na on the TiO_2 NFs exhibited enhanced absorbance in just the visible region. The probability of visible absorption may be due to the C impurities in the pristine TiO_2 NFs, created during the synthesis process. The distinct spectra clearly demonstrate the effective role of S in the TiO_2 NFs, causing the enhancement of the visible absorbance behavior that was further extended with the presence of Na in the Na/S-TiO_2 NFs. Surface functionalization of TiS_3 (a narrow band gap semiconductor) on the TiO_2 NFs plays a sufficient role in the absorbance towards the visible region. The effect of S and Na/S on the TiO_2 NFs manifests as a broadened absorption onset at 2.58 eV and 2.28 eV, respectively, which can be interpreted in terms of type-II core–shell structures or an interface, allowing access to visible wavelengths that would not be possible with one of the two materials (either core or shell) alone. The shift of the absorption onset from 3.14 eV (TiO_2 NFs) to the longer wavelength of <2.6 eV with the broadened absorption edge reveals the effect of the substitution of TiS_3 or S, including the signature band alignment, under the sulfidation process. The extended absorption of the Na/S-TiO_2 NFs with sulfur functionalization reveals the diffusion of S ions and Na functionalization leads to a maximized interfacial contact of Ti and S ions at the interface and influences the band function. The effect of the S modification leading to retardation in the recombination rate of photoinduced charge carriers and the considerable harvest of light energy in the visible region are discernible from the DRS results.

Fig. 7 shows the fluorescence spectra of the S and Na/S-TiO_2 NFs at the excitation wavelength of 350 nm. The sharp emission at 397 nm represents the band edge emission, which is attributed to the quasi-free recombination at the absorption band edge of the TiO_2 NFs. Broad emissions at around 430 nm and

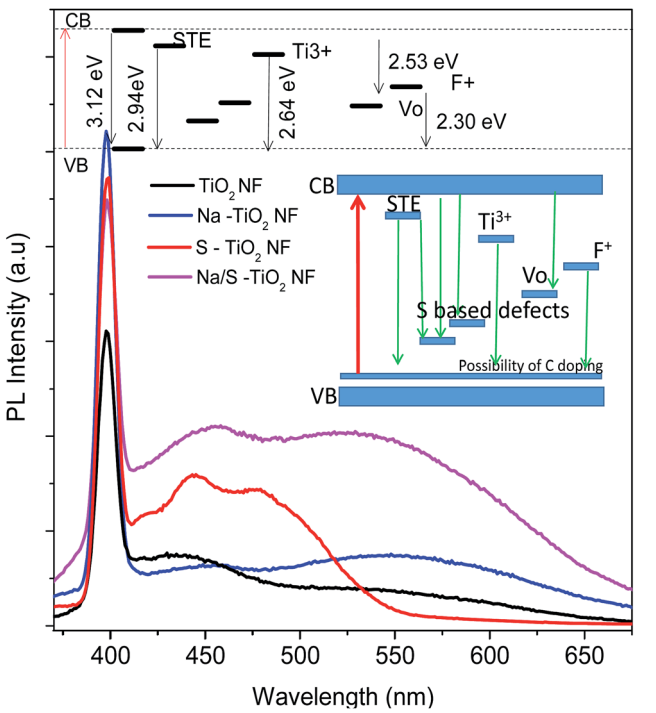

Fig. 7 Room temperature photoluminescence spectra of the pristine TiO_2 NFs and surface modified TiO_2 NF samples under an excitation of 350 nm.

540 nm represent shallow and deep trap states near and below the band edge,[36] and these emissions represent surface state emissions. These surface states are localized within the band gap and are induced as traps to excite electrons at the higher wavelength. From the XPS results, we found that the sulfidation process induced passivated traps that anticipated the visible emission. To gain a deep understanding of the density and position of defects and trap states, PL spectra were deconvoluted with Gaussian fitting[37] (Fig. S9†). The pristine TiO_2 NFs reveal a promising excitonic emission at 397 nm representing the band edge emission. The peak at around 420–430 nm was associated with self-trapped excitons (STE) located at TiO_6 octahedra, arising due to the interaction of conduction band electrons localized in the Ti 3d orbitals with holes present in the O 2p orbitals of TiO_2, which were all over the modified TiO_2 NFs. These are donor type oxygen vacancy states, present below the conduction band.[37] The broad emission at around 540 nm was associated with deep trap emission, which was associated with F centers (O_{V+} and O_{V++}).[37,38] Upon modifying the TiO_2 NF surface with Na and S, the surface state emissions at 433 nm, 444 nm, 479 nm and 540 nm became intense, due to the increased recombination of trapped electrons and holes arising from dangling bonds and impurities in the TiO_2 NFs. The emission peaks at around 470 and 540 nm were ascribed to oxygen vacancy related trap states. These were due to the oxygen vacancies associated with Ti^{3+} in anatase TiO_2. As for the role of Na, surface diffusion induced the formation of F-centers, which enhanced the trapping of electron pairs in the vacant cavity due to the loss of an O atoms in the TiO_2 lattice.

The emissions due to Ti^{3+} and F^+ centers arise because of the occupation of one electron in the F-center of a neighboring Ti^{4+} ion,[39,40] initiated by the sulfidation process. The oxygen vacancies and surface hydroxyl groups are dominant sites for trapped electrons and holes. These trapped carriers are captured by oxygen vacancies and surface hydroxyl groups, contributing to the visible luminescence of the Na/S-TiO_2 NFs. However, after the sulfidation process, the additional intense emission at 444 nm was found to be due to S interstitial-based defect sites in the S-TiO_2 NFs. Furthermore, there is an additional emission at around 458 nm in the Na and S co-catalyst TiO_2 NFs that reveals the additional interaction of Na ions with the S^{2-}- or SO^{3-}-based defects. A green emission observed at around 490 nm arises due to the charge transition from the conduction band to oxygen vacancies or donor–acceptor recombination states.[41] By comparing the different forms of surface modification, it can be understood that the sulfidation process initiates sulfur-based defect sites and induces Na ion functionalization, due to oxygen vacancies associated with Ti^{3+} defect states. Photoluminescence is a surface phenomenon, and modification of the TiO_2 NF surface with Na and S significantly affects the fluorescence emission.

The catalytic behavior of the surface-modified TiO_2 NFs was investigated under UV and visible irradiation, using RhB as a probe molecule with respect to time. As compared to the pristine TiO_2 NFs, the surface-modified NFs had a higher absorption rate, due to the electrostatic interaction of the S impurities with the dye molecules and the enhanced number of surface interactive sites (Fig. 8). Extending the equilibrium time to 3 h under darkness did not influence the RhB concentration (Fig. S10†), which indicated inactivity of the catalyst under dark. In this process, the Na and S co-catalyst TiO_2 NFs had a higher dye absorption rate at the equilibrium state, which reveals the higher surface interaction on the surface-modified NFs than that of the pristine one, due to the diffusive nature of the sulfur-decorated shell wall. In the absence of a catalyst, the RhB solution showed a self-degradation ability of nearly 13% in 180 min under photo-illumination (Fig. S10†) and the photoresponsive catalytic behavior of the RhB solution is shown in the Fig. S11 and S12.† Fig. 8a shows RhB degradation efficiencies of 79.89%, 85.76%, 95.30%, 98.40% and 57.82% for the pristine TiO_2 NFs, Na–TiO_2 NFs, S-TiO_2 NFs, Na/S-TiO_2 NFs and commercial Degussa P25, respectively, under UV irradiation for 90 min. Fig. 8b shows that on irradiating the surface-modified TiO_2 NF nanostructures under visible-light, they exhibited RhB degradation efficiencies of 45.12%, 54.83%, 79.59%, 97.09% and 19.17%, for pristine TiO_2 NFs, Na–TiO_2 NFs, S-TiO_2 NFs, Na/S-TiO_2 NFs, and Degussa P25, respectively, for 90 min. Table S2† displays the photoresponsive properties of the surface-modified TiO_2 NF samples. The pristine TiO_2 NFs exhibited a higher catalytic activity than the Degussa P25 catalyst under UV and visible irradiation. Pristine TiO_2 and the Na–TiO_2 NFs showed visible-light photodegradation activities of around 45% and 54%, respectively, due to carbon doping in the TiO_2 nanograins during the synthesis process, which promoted a narrow band function and initiated catalytic behavior under visible-light.[42] As compared to the pristine TiO_2 NFs, the TiO_2 NFs sulfidated with the TAA and Na_2S precursors showed higher visible-light catalytic activity. The results show that the S-TiO_2 NFs (TAA as precursor) exhibited a visible-light catalytic efficiency of around 80% in 90 min. Furthermore, upon using Na_2S as the precursor during sulfidation, Na and S modification occurred on the TiO_2 surface, and the Na/S-TiO_2 NFs exhibited an efficient visible-light photocatalytic activity of 97% in 90 min. Varying the surface modification induced visible-light absorption capability on the TiO_2 NFs, and the nature of the S impurities present played a critical role in enhancing the catalytic performance. The effect on the visible photocatalytic activity was clearly evidenced by the optical response of the modified surface, which was confirmed by the UV and PL results (Fig. 6 and 7).

Owing to the charge transfer process in the S-TiO_2 NFs, the sulfur defect states occupied the band position on the TiO_2 and favored the visible absorption. Meanwhile, the conduction band of the surface TiS_3 nanograins, deformed through sulfidation, lies at a more negative potential than that of TiO_2, while the valence band of TiO_2 is more positive than that of TiS_3, which favors the formation of a type II band structure. Under photoirradiation, photogenerated electrons pass from the conduction band of TiS_3 to the conduction band of TiO_2 and hole transfer occurs from the valence band of TiO_2 to the sulfur defect states, or to the valence band of TiS_3, initiating carrier separation and resulting in the formation of highly oxidative hydroxyl radical species ($OH^{\bullet}$) and super oxide ions ($O_2^{\bullet}$). Fig. 8c and d show the photodegradation reaction kinetics of the

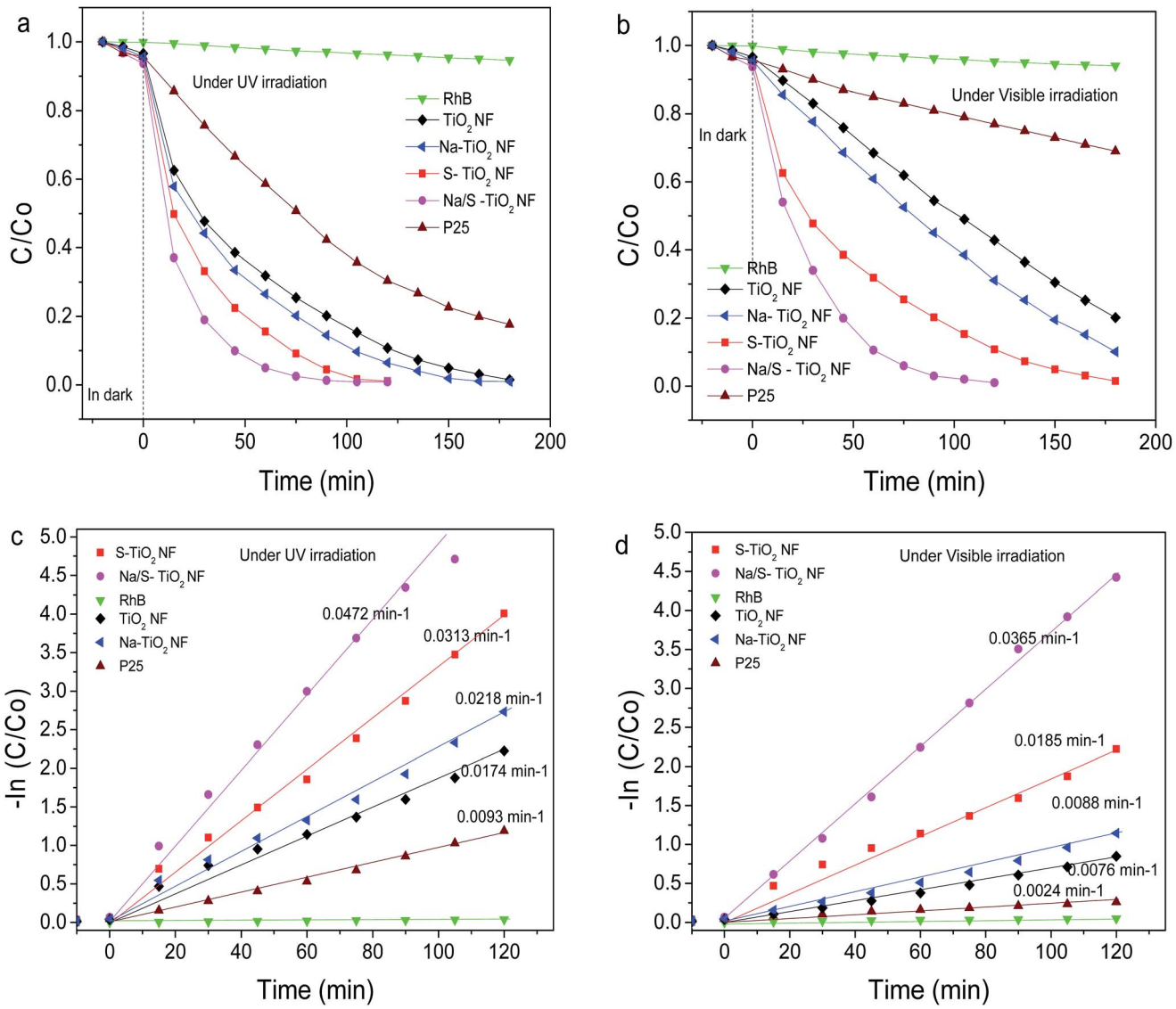

Fig. 8 Photodegradation performance and degradation rate of the RhB under (a and c) UV and (b and d) visible-light ($\lambda > 400$ nm) for pristine TiO_2 NFs, Na–TiO_2 NFs, S-TiO_2 NFs and Na/S-TiO_2 NFs.

surface-modified TiO_2 NFs, which follow the first-order rate law, as shown by the highly linear plot of $\ln(C/C_0)$ against the irradiation time (t). Under visible irradiation, Na/S-TiO_2 NFs exhibited the highest apparent rate constant, determined to be 0.0365 min^{-1}, which is about 4.8 times, 4.1 times and 1.9 times higher than that of pure TiO_2 NFs (0.0076 min^{-1}), Na–TiO_2 NFs (0.0088 min^{-1}) and S-TiO_2 NFs (0.0185 min^{-1}) respectively, revealing the superior visible photocatalytic activity of S-TiO_2 NFs with the effect of Na and TiS_3 shell interface. Even under UV irradiation, Na/S-TiO_2 NFs had the highest reaction rate (k = 0.0472 min^{-1}), which is nearly 2.7 times higher than the rate for the pure TiO_2 NFs (k = 0.0174 min^{-1}) and 2.1 and 1.5 times higher than that for the Na–TiO_2 NFs (0.0218 min^{-1}) and S-TiO_2 NFs (0.0313 min^{-1}), respectively. The promising photocatalytic degradation rate of the TiO_2 NFs under UV irradiation was responsible for its band function, and the S and Na modification improved the carrier separation rate. However, the visible-light catalytic behavior of the TiO_2 NFs revealed the role of Na inclusion and S-based defect levels in the induction of visible-light absorption. Additionally, the surface modification improved the adsorption ratio of the dye molecules as compared with the pristine TiO_2 NFs, initiating a greater interaction with the dye molecules on the surface. This may be due to the chemisorbed oxygen or oxygen vacancy sites on the surface of the NFs, which was confirmed by the XPS results. Further catalytic properties were verified by investigating the decomposition of MB and 4-chlorophenol (4-CP), and were evaluated by monitoring the absorption spectra (Fig. S13†). The results reveal the ability of the surface-modified TiO_2 NFs in degrading the selected organic pollutants under visible irradiation. The degradation efficiency of TiO_2, and Na/S-TiO_2 NFs for MB and 4-CP were calculated to be 24.3% and 97.6% in 120 min and 27.7% and 51.1% in 120 min, respectively, under visible irradiation.

For the two components (MB and 4-CP), the degradation results were similar to that of RhB, with fast degradation efficiency for Na/S-TiO_2 NFs. Under visible irradiation, there is the possibility of a sensitization effect due the light absorbed by the dye molecules, thereby transferring electrons to the catalytic surface. However, that does not play a big role here because the degradation of the three components (RhB, MB and 4-CP) showed a similar degradation trend (4-CP is not a dye). RhB and MB exhibited a faster degradation rate, 1.2 times greater than that of 4-CP, and this high decomposition rate may be due to the sensitization effect. The commendable visible-light catalytic performance of the Na/S-TiO_2 NFs as compared with the pristine and S-TiO_2 NFs could be due to the formation of Ti–S and S–O on the catalytic surface, promoting carrier separation efficiency. The sulfur modification on the TiO_2 NFs acts as the TiO_2–Ti/S/O core–shell interface, which improves the visible-light absorption due to the presence of S-based defect bands that narrow the band function of TiO_2 from 3.2 eV to 2.3 eV. The diffusion of Na on the TiO_2 NFs makes a pathway for sulfur to diffuse through the catalytic surface and increases the interaction of S with the TiO_2 NFs. However, this phenomenon happened while using Na_2S as the sulfidation precursor. When TAA is used as the sulfidation precursor, S ions interact with the Ti ions and form some TiO_2–Ti/S interfaces. However, mainly S ions interacted with the TiO_2 NFs and deformed the crystallinity of the TiO_2 NF nanograins and formed S–Ti bonds only at the surfaces of many amorphous grains. The presence of the S ion on the TiO_2 NFs with the two different sulfidation precursors was clearly revealed from the XPS results. However, the reason behind the different types of interactions observed when using the respective precursors (TAA, Na_2S) is not yet clearly understood. The presence of S-based defect states narrowed the band function of TiO_2 and improved the visible-light photocatalytic efficiency. One of the major factors that was accountable during photocatalysis was the interaction of S ions with Ti, forming a type II band between O–Ti and Ti–S, which promoted the movement of carriers through the interface and also offered effective passivation of the TiO_2 core surface.

Furthermore, the presence of S-based defects on the TiO_2 surface favored the additional degree of freedom to enhance the spectral response. We were not able to confirm a core–shell geometry because of the assembly of nanograins. However, the interaction of sulfur initiated the spatial transition in the visible region, which enhanced the visible absorption and decelerated charge carrier recombination. The interaction of S–O ions favored the creation of oxygen vacancies, which effectively delayed the carrier recombination rate. To validate the possibility of the carrier transport, the band positions of the conduction and valence band were calculated for the surface modified TiO_2 NFs. The presence of surface states that favored the band gap reduction was understood by identifying the conduction and valence band positions of the surface modified TiO_2 NFs. Therefore, valence band (VB) XPS of the surface modified TiO_2 NFs was examined, as shown in Fig. 9 and tabulated in Table S3.† The VB Density of States (DOS) maximum of the pristine TiO_2 NFs was observed with the edge of the maximum energy of 2.54 eV. The measured band gap of

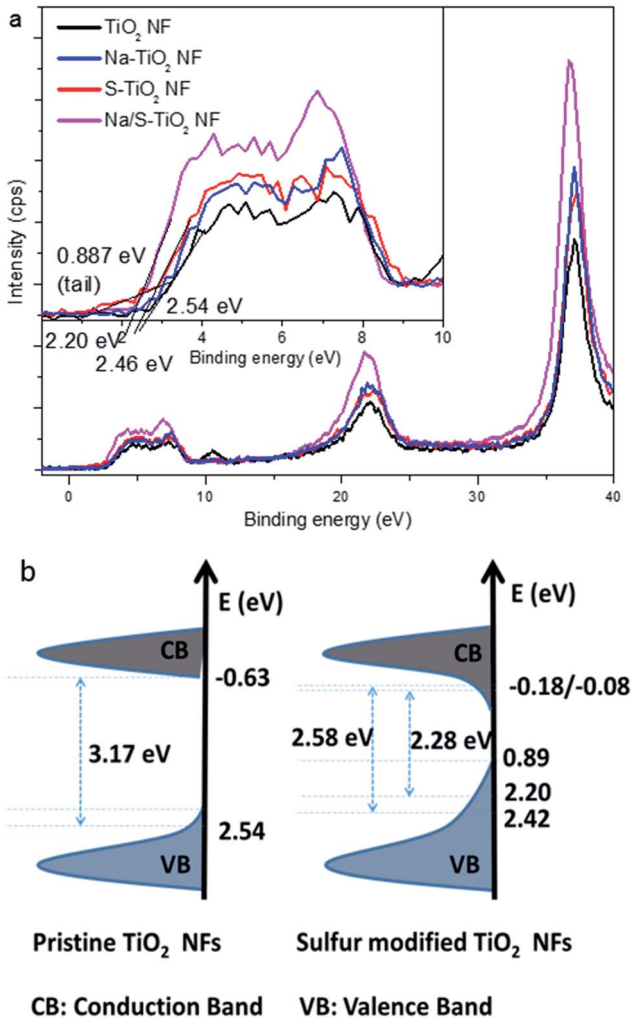

Fig. 9 (a) Valence-band XPS spectra of the pristine TiO_2 NFs and surface modified TiO_2 NFs. (b) Schematic illustration of the DOS of the S-TiO_2 NFs, compared to that of the pristine TiO_2 NFs.

the pristine TiO_2, which is around 3.17 eV (Fig. 6), reveals that the position of the conduction band minimum would occur at −0.63 eV. Upon modifying TiO_2, the VB maximum energy shifted to the lower binding energies of ~2.42 and ~2.20 eV for the S-TiO_2 NFs and Na/S-TiO_2 NFs, respectively, which was followed by a band tail towards ~0.89 eV. Correlating these results with the optical measurements, suggests narrow band functions with CB minimums of ~0.18 and ~0.08 eV exhibited by the S-TiO_2 NFs and Na/S-TiO_2 NFs, respectively. As represented by the schematic illustration in the Fig. 9, the DOS of the S-TiO_2 NFs reveals the narrowing of the band function. Surface disorder and the defective core–shell form of the TiO_2-based nanostructures induced a narrow band gap of up to 1.8 eV.[43,44]

Here, the sulfidation of TiO_2 NFs effectively introduced surface defects (oxygen vacancies, sulfur defects) on the TiO_2 NF surface, which narrowed the band gap, as predicted by the slight VB tailing. The upper lift in the VB position is due to the disorder formation of shell surface on the TiO_2 NFs.[45] The creation of localized surface states through oxygen vacancies

and Ti^{3+} formation narrows the band function by minimizing the CB position. Further, S defect bands can cause band narrowing in the TiO_2 NFs, with the slight tails in the VB position followed by the conduction band minima. The decrease in the band function due to the surface modification was attributed to both the raising of the VB position (surface disorder) and the lowering of the CB (O_V and Ti^{3+} defect states).[44] Upon modifying with S through the TAA-based sulfidation process, the presence of surface disorder arose due to the modification of S defect states tailing the VB position. In addition, upon modifying the TiO_2 NFs using the Na_2S-based sulfidation process, diffusion of Na followed by S ions initiated the tailing of the valence band through the surface disorder effect, creation of oxygen vacancies and presence of Ti^{3+}, inducing the tailing of the CB position, which extended below the CB minima.

Based on the experimental results, a possible catalytic mechanism was proposed for the visible photocatalytic properties of S-TiO_2 NFs and Na/S-TiO_2 NFs, which is represented in Fig. 10. The thin layered or surface-decorated TiS_3 nanograins on the TiO_2 NFs reveal the transfer of photogenerated electrons to TiO_2 at the grain interface. Electrons move from the CB of TiS_3 to the CB of TiO_2 due to the negative potential of the TiS_3 nanograins. However, a trace amount of TiS_3 nanograins do not contribute much to the enhanced performance of the surface-modified TiO_2 NFs under visible-light irradiation. The presence of S impurities and the creation of oxygen vacancies improved the photo-induced charge carrier production at the surface of the S-TiO_2 NFs. Owing to the narrow band function due to the sulfur defect level, the collection and transportation of photogenerated charge carriers were improved, as reflected in Fig. 10. By doping TiO_2 with S, visible-light catalytic ability was induced through the formation of S 3p states as a CB between the O 2p–Ti 3d state.[46]

This induced the promotion of electron-occupied states above the VB of the TiO_2 nanostructures, which led to the narrowing of the band function in sulfur-modified TiO_2. Modifying the TiO_2 with sulfur narrows the band function up to 1.7 eV (ref. 47) and the presence of S impurities over the TiO_2 nanostructures increases the band narrowing function due to the increased presence of S^{4+}/S^{6+} impurity states. The sulfur-based impurities favored the production of hydroxyl radicals by reducing the recombination rate towards the visible-light catalytic behavior.[48,49] In our work, the HRTEM images (Fig. 4) exhibit trace amounts of TiS_3 nanograins as a function of sulfidation, which lead to the narrowing of the band function at the surface interface. As observed from the XPS and PL spectra (Fig. 5 and 7), there were S-based surface states which are favorable for the visible-light response and improve the visible-light catalytic behavior. The Ti–S–O interaction favored the effective visible absorption and promoted the carrier separation rate. In the S-TiO_2 NFs, the presence of S^{2-} at the surface promoted the visible-light catalytic behavior and diffusing nature of the S^{2-}- and SO^{3-}-based defect states created in the Na/S-TiO_2 NFs, leading to effective visible-light catalytic behavior. Na showed no significant role in improving the carrier mobility in the TiO_2 NFs, but it played a crucial role in improving the oxygen vacancies (F+ centers), which may lower the band function and act as surface traps for delaying the carrier recombination. During the sulfidation process, Na diffuses through the TiO_2 NFs and creates a path for more S to create a diffuse shell wall on the TiO_2 NFs. This reveals that the present nature of the S-based surface defects states is a crucial factor behind the visible-light photocatalytic behavior.

The catalytic performance of a semiconductor is enhanced based on the production of reactive oxygen species through the separation of photogenerated charge carriers. In order to understand the mechanism behind how S-modification enhances the visible-light catalytic behavior, quantifying the production of reactive oxygen species during the catalytic process was deemed necessary. The rate of O_2^- production on the sulfidated TiO_2 NFs (Fig. S14†) was quantified through the quenching rate of NBT under photo-irradiation. When compared with the pristine TiO_2 NFs, the sulfidated TiO_2 NFs exhibited a higher reduction rate of NBT, which reveals the enhanced production rate of O_2^- over the catalyst surface after sulfidation process. The production rate of hydroxyl radicals ($^{\bullet}OH$) under photo-irradiation crucially decides the catalytic performance. Fig. S15† displays the hydroxyl radical ($^{\bullet}OH$) quantification experiment of active species during the photocatalytic reaction of sulfidated TiO_2 NFs under visible irradiation. The production rate of hydroxyterephthalic acid from the terephthalic acid was quantified by the generation of $^{\bullet}OH$ through the catalyst. The production rate of $^{\bullet}OH$ was quantified through the luminescence intensity from the pristine NFs, as well as the S-TiO_2 NFs, and the transformation rate was in the order Na/S-TiO_2 > S-TiO_2 > Na–TiO_2 > TiO_2 under visible-light irradiation. While modifying the TiO_2 NFs with the S^{2-}- and SO^{3-}-based defect states, there was a considerable increase in the production of $^{\bullet}OH$.

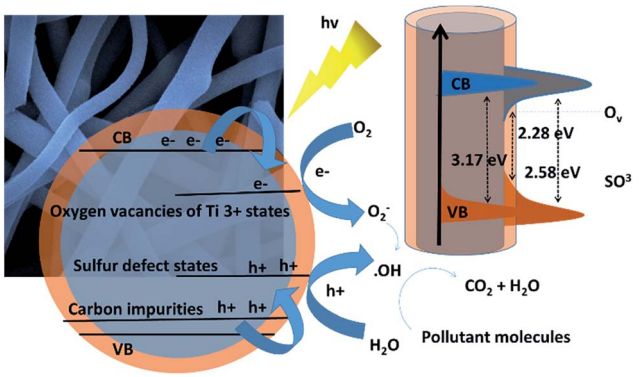

Fig. 10 Band diagram and the proposed mechanism for the dye degradation by the sulfidated TiO_2 NFs.

$$TiS_3 + h\nu \rightarrow TiS_3\,(e_{CB}^{-}\cdots h_{VB}^{+})$$

$$TiS_3\,(e_{CB}^{-}) + TiO_2 \rightarrow TiS_3 + TiO_2\,(e_{CB}^{-})$$

$$TiO_2 + h\nu \rightarrow TiO_2\,(e_{CB}^{-}\cdots h_{VB}^{+})$$

$$TiO_2\,(e_{CB}^{-}) + O_2 \rightarrow TiO_2 + O_2^{\bullet -}$$

$$O_2^{\bullet -} + H_2O \rightarrow HO_2 + OH^-$$

$$HO_2 + H_2O \rightarrow OH^{\bullet} + H_2O_2$$

$$H_2O_2 \rightarrow 2OH^{\bullet}$$

$$OH + MB \rightarrow H_2O + CO_2$$

$$TiO_2\ (h_{VB}^+) + RhB \rightarrow \text{degraded product}$$

Sulfur modification on the TiO_2 NFs promoted the visible-light catalytic properties through the effective production of $^{\bullet}OH$ radicals, by narrowing the band function. Trace amount of TiS_3 nanograins and sulfur-based defect sites promoted the visible-light absorption and created the photoexcited reactive species. The excited electrons from the TiS_3 nanograins were transferred to the CB band of TiO_2, and the promotion of sulfur states narrowed the band function, leading to the transfer of the photogenerated holes from the VB of TiO_2 to the sulfur-based defect states. The effective migration of the carriers delayed the recombination rate of the photoinduced charge carriers. The superoxide radicals ($O_2^{\bullet -}$) were generated by the interaction of photogenerated electrons with molecular oxygen (O_2), which consecutively resulted in the formation of hydroxyl radicals in the reaction system, inducing the photodegradation of RhB. The valence band holes were also engaged in the photocatalytic process to a slight extent, as supported by the trapping experiments. This may favor the production of singlet oxygen, due to the probability of the mid-band function by the surface defect states. Thus, the above findings allowed us to conclude that the hydroxyl radicals ($^{\bullet}OH$) are the ruling active species (resulting from superoxide radical anions, which in turn are formed by conduction band electrons) with favorable assistance from the valence band holes in the degradation of RhB using the S-TiO_2 NFs under visible-light illumination. The stability of the catalyst upon light irradiation is highly important, thus the catalytic degradation was performed for five repeat cycles (Fig. S16†). After the catalytic process, the catalyst was washed with water and used in the subsequent cycles. The degradation efficiency rate for the fifth test was nearly 89% of the first test, which revealed the catalytic stability of the surface modified NFs. The loss in the catalytic performance may be due to the interaction of photogenerated holes with sulfur impurity states or surface oxygen atoms, which led to the decrease in catalytic activity. This may also be due to unpreventable catalyst loss in the recycling process. The catalytic stability was much greater than that for the pristine TiO_2 NFs. As illustrated from the SEM and XPS results, there is no discernible change in the surface morphology (Fig. S17†), but the chemical states after five successive cycles of photocatalysis lost little of its functional group concentration (Fig. S18†). The high resolution XPS analysis of the samples prove that there is a decrease in the oxygen vacancy and sulfur state ratio after the five successive catalytic cycles, as illustrated in Fig. S18.† However, there is no significant shift in the catalytic surface states when compared with the samples before photo-irradiation. The findings confirm that the decrease in the catalytic efficiency during the catalytic cycles may be due to the loss of the shell layer functionality. Further improvements to inhibit the photocorrosion of the catalytic surface present a challenge, and more efforts are needed to provide a solution to this issue. We anticipate that our work has improved the visible-light catalytic behavior of the TiO_2 NFs through surface modification, and we have demonstrated efficacious and recyclable performance.

Conclusion

Through sulfidation, electrospun TiO_2 NFs were chemically modified and formed TiS_3-decorated TiO_2 NFs. By varying the different sulfidation precursors, the surface interaction was tuned with the aid of Na diffusion. The visible photocatalytic activity of the TiO_2 NFs was investigated with respect to the role of S- and Na/S-based surface modification. Through the sulfidation process, sulfur states and the oxygen defect states arose on the TiO_2 NF surface, leading to enhanced visible-light absorption and improved catalytic behavior. The interaction of S ions with Ti–O created oxygen vacancies that served as electron traps, which delayed the recombination rate at the surface, favoring the movement of photogenerated charge carriers to the surface to engage in catalytic activity. The role of oxygen vacancies and sulfur-induced states was to narrow the band function to 2.2 eV and improve the activity of the materials under visible-light irradiation.

Acknowledgements

K. S. Ranjith acknowledges The Scientific & Technological Research Council of Turkey (TUBITAK), BIDEB 2216-Fellowships for Research Fellowship Programme for Foreign Citizens, for the postdoctoral fellowship. T. Uyar acknowledges The Turkish Academy of Sciences – Outstanding Young Scientists Award Program (TUBA-GEBIP), Turkey for partial funding.

References

1 V. Etacheri, C. D. Valentin, J. Schneider, D. Bahnemann and S. C. Pilla, *J. Photochem. Photobiol., C*, 2005, **25**, 1–29.
2 H. Yan, X. Wang, M. Yao and X. Yao, *Prog. Nat. Sci.: Mater. Int.*, 2013, **23**, 402–407.
3 S. Kurian, H. Seo and H. Jeon, *J. Phys. Chem. C*, 2013, **117**, 16811–16819.
4 S. George, S. Pokhrel, Z. Ji, B. L. Henderson, T. Xia, L. J. Li, J. I. Zink, A. E. Nel and L. Mädler, *J. Am. Chem. Soc.*, 2011, **133**, 11270–11278.
5 R. Long, N. J. English and O. V. Prezhdo, *J. Phys. Chem. Lett.*, 2014, **5**, 2941–2946.
6 F. M. Pesci, G. Wang, D. R. Klug, Y. Li and A. J. Cowan, *J. Phys. Chem. C*, 2013, **117**, 25837–25844.
7 Y. Xia, P. Yang, Y. Sun, Y. Wu, B. Mayers, B. Gates, Y. Yin, F. Kim and H. Yan, *Adv. Mater.*, 2003, **15**, 353–389.
8 J. Y. Cheng, F. Zhang, V. P. Chuang, A. M. Mayes and C. A. Ross, *Nano Lett.*, 2006, **6**, 2099–2103.

9 S. A. Ansari, M. M. Khan, M. O. Ansari and M. H. Cho, *New J. Chem.*, 2016, **40**, 3000–3009.
10 T. Ohno, M. Akiyoshi, T. Umebayashi, K. Asai, T. Mitsui and M. Matsumura, *Appl. Catal., A*, 2004, **265**, 115–121.
11 L. Kong, C. Wang, H. Zheng, X. Zhang and Y. Liu, *J. Phys. Chem. C*, 2015, **119**, 16623–16632.
12 M. Dahl, Y. Liu and Y. Yin, Composite Titanium Dioxide Nanomaterials, *Chem. Rev.*, 2014, **114**, 9853–9889.
13 Y. Wang, Q. Wang, X. Zhan, F. Wang, M. Safdar and J. He, *Nanoscale*, 2013, **5**, 8326–8339.
14 I. J. Ferrer, J. R. Ares, J. M. Clamagirand, M. Barawi and C. Sanchez, *Thin Solid Films*, 2012, **535**, 398–401.
15 K. S. Ranjith, A. Senthamizhan, B. Balusamy and T. Uyar, *Catal. Sci. Technol.*, 2017, **7**, 1167–1180.
16 J. Rouhi, M. H. Mamat, C. H. R. Ooi, S. Mahmud and M. R. Mahmood, *PLoS One*, 2015, **10**, e0123433.
17 L. Wanga, X. Duana, G. Wang, C. Liua, S. Luoa, S. Zhanga, Y. Zenga, Y. Xua, Y. Liuc and X. Duan, *Appl. Catal., B*, 2016, **186**, 88–96.
18 J. Wu, D. Wang, H. Liu, W. M. Lau and L. M. Liu, *RSC Adv.*, 2015, **5**, 21455–21463.
19 J. O. Island, M. Buscema, M. Barawi, J. M. Clamagirand, J. R. Ares, C. Sánchez, I. J. Ferrer, G. A. Steele, H. S. J. van der Zant and A. C. Gomez, *Adv. Opt. Mater.*, 2014, **2**, 641–645.
20 I. J. Ferrer, J. R. Ares, J. M. Clamagirand, M. Barawi and C. Sánchez, *Thin Solid Films*, 2013, **535**, 398–401.
21 A. J. M. Mendoza, M. Barawi, R. Biele, E. Flores, J. R. Ares, C. Sánchez, G. R. Bollinger, N. Agraït, R. D'Agosta, I. J. Ferrer and A. C. Gomez, *Adv. Electron. Mater.*, 2015, **1**, 1500126.
22 M. Zhu, C. Zhai, L. Qiu, C. Lu, A. S. Paton, Y. Du and M. C. Goh, *ACS Sustainable Chem. Eng.*, 2015, **3**, 3123–3129.
23 S. W. Shin, J. Y. Lee, K. S. Ahn, S. H. Kang and J. H. Kim, *J. Phys. Chem. C*, 2015, **119**, 13375–13383.
24 W. Liu, F. Xiu, K. Sun, Y. H. Xie, K. L. Wang, Y. Wang, J. Zou, Z. Yang and J. Liu, *J. Am. Chem. Soc.*, 2010, **132**, 2498–2499.
25 H. He, S. Lin, G. Yuan, L. Zhang, W. Zhang, L. Luo, Y. Cao, Z. Ye and S. T. Lee, *J. Phys. Chem. C*, 2011, **115**, 19018–19022.
26 S. Naraginti, Y. Li, Y. Wu, C. Zhang and A. R. Upreti, *RSC Adv.*, 2016, **6**, 87246–87257.
27 F. D. Hardcastle, H. Ishihara, R. Sharma and A. S. Biris, *J. Mater. Chem.*, 2011, **21**, 6337–6345.
28 J. Wang, Q. Zhang, S. Yin, T. Sato and F. Saito, *J. Phys. Chem. Solids*, 2007, **68**, 189–192.
29 J. Yang, H. Bai, Q. Jiang and J. Lian, *Thin Solid Films*, 2008, **516**, 1736–1742.
30 B. Bharti, S. Kumar, H. N. Lee and R. Kumar, *Sci. Rep.*, 2016, **6**, 32355.
31 T. Ohno, T. Tsubota, M. Toyofukum and R. Inaba, *Catal. Lett.*, 2004, **98**, 255–258.
32 X. Jiang, Y. Zhang, J. Jiang, Y. Rong, Y. Wang, Y. Wu and C. Pan, *J. Phys. Chem. C*, 2012, **116**, 22619–22624.
33 N. Li, X. Zhang, W. Zhou, Z. Liu, G. Xie, Y. Wang and Y. Du, *Inorg. Chem. Front.*, 2014, **1**, 521–525.
34 S. M. Prokes, J. L. Gole, X. Chen, C. Burda and W. E. Carlos, *Adv. Funct. Mater.*, 2005, **15**, 161–167.
35 P. Xu, T. Xu, J. Lu, S. Gao, N. S. Hosmane, B. Huang, Y. Dai and Y. Wang, *Energy Environ. Sci.*, 2010, **3**, 1128–1134.
36 B. Choudhury, M. Dey and A. Choudhury, *Appl. Nanosci.*, 2014, **4**, 499–506.
37 Y. Lei, L. D. Zhang, G. W. Meng, G. H. Li, X. Y. Zhang, C. H. Liang, W. Chen and S. X. Wang, *Appl. Phys. Lett.*, 2001, **78**, 1125–1127.
38 A. Ghobadi, T. G. Ulusoy, R. Garifullin, M. O. Guler and A. K. Okyay, *Sci. Rep.*, 2016, **6**, 30587.
39 S. Song, Z. Sheng, Y. Liu, H. Wang and Z. Wu, *J. Environ. Sci.*, 2012, **8**, 1519–1524.
40 A. K. Tripathi, M. C. Mathpal, P. Kumar, V. Agrahari, M. K. Singh, S. K. Mishra, M. M. Ahmad and A. Arvind, *Adv. Mater. Lett.*, 2015, **3**, 201–208.
41 A. S. Ganeshraja, K. Rajkumar, K. Zhu, X. Li, S. Thirumurugan, W. Xu, J. Zhang, M. Yang, K. Anbalagan and J. Wang, *RSC Adv.*, 2016, **6**, 72791–72802.
42 F. Dong, S. Guo, H. Wang, X. Li and Z. Wu, *J. Phys. Chem. C*, 2011, **115**, 13285–13292.
43 X. Chen, L. Liu, P. Y. Yu and S. S. Mao, *Science*, 2011, **331**, 746–750.
44 A. Naldoni, M. Allieta, S. Santangelo, M. Marelli, F. Fabbri, S. Cappelli, C. L. Bianchi, R. Psaro and V. Dal Santo, *J. Am. Chem. Soc.*, 2012, **134**, 7600–7603.
45 Q. Kang, J. Cao, Y. Zhang, L. Liu, H. Xu and J. Ye, *J. Mater. Chem. A*, 2013, **1**, 5766–5774.
46 T. Ohno, M. Akiyoshi, T. Umebayashi, K. Asai, T. Mitsui and M. Matsumura, *Appl. Catal., A*, 2004, **265**, 115–121.
47 C. McManamon, J. O'Connell, P. Delaney, S. Rasappa, J. D. Holmes and M. A. Morris, *J. Mol. Catal. A: Chem.*, 2015, **406**, 51–57.
48 P. V. R. K. Ramacharyulu, D. B. Nimbalkar, J. Praveen Kumar, G. K. Prasad and S. C. Ke, *RSC Adv.*, 2015, **5**, 37096–37101.
49 R. G. Chaudhuri and S. Paria, *Dalton Trans.*, 2014, **43**, 5526–5534.